

# The Carnegie RR Lyrae Program: The Mid-Infrared RR Lyrae Period-Luminosity-Metallicity Relations in $\omega$ Cen

Meredith J. Durbin<sup>1</sup> Victoria Scowcroft<sup>2</sup> Wendy L. Freedman<sup>3</sup> Barry F. Madore<sup>2</sup>  
 Rachael L. Beaton<sup>2</sup> Andrew J. Monson<sup>4</sup> Mark Seibert<sup>2</sup>

<sup>1</sup> Department of Astronomy, University of Washington, Seattle, WA 98195, USA

<sup>2</sup> Observatories of the Carnegie Institution of Washington, 813 Santa Barbara St., Pasadena, CA 91101, USA

<sup>3</sup> Department of Astronomy and Astrophysics, University of Chicago, 5640 S Ellis Ave, Chicago, IL 60637, USA

<sup>4</sup> Department of Astronomy and Astrophysics, The Pennsylvania State University, 403 Davey Lab, University Park, PA, 16802, USA

Accepted XXX. Received YYY; in original form ZZZ

## ABSTRACT

[abstract]

**Key words:** keyword1 - keyword2 - keyword3

## 1 INTRODUCTION

The Carnegie RR Lyrae Program (CRRP) is a Warm *Spitzer* program (Freedman et al. 2012a, PID 90002) which aims to provide an independent, population II measurement of the Hubble constant ( $H_0$ ), tied to RR Lyrae variables with high precision geometric distances in the Milky Way. Similar to the Carnegie Hubble Program (CHP Freedman et al. 2011), CRRP will provide a single instrument measurement of  $H_0$ . This will provide important constraints on the external accuracy of the standard candle distance ladder, and the internal consistency of the distance measurements of Cepheids and RR Lyrae variables.

In the era of ‘precision cosmology’ it is important to fully understand all sources of uncertainty in our experiments. Although the results distance ladder measurements such as Riess et al. (2011) and Freedman et al. (2012b) agree very well, when we consider the latest results from *Planck* there is tension. The *Planck* study derives its measurement from a model of the cosmic microwave background (CMB), so is completely independent of the Riess et al. and Freedman et al. results. Works such as Rigault et al. (2015) and Efstathiou (2014) have examined the contribution of systematic uncertainties at the far end of the distance ladder to this tension. The CRRP is quantifying the systematic uncertainty in the standard candle distance ladder by making meaningful comparisons at the base of the Cepheid and RR Lyrae distance ladders in the mid-infrared, where distance measurements of similar precision are achievable.

A good local standard candle (as defined by Aaronson & Mould 1986) has the following features: a) a physical basis, b) objective measurables, c) minimal corrections, and d) small scatter. RR Lyrae variables (hereafter RRL) are excellent standard candles in the mid-infrared. As Longmore et al. (1986) demonstrated, unlike at optical wavelengths

where their absolute magnitudes depend only on metallicity, in the infrared RRL follow a clear period–luminosity (PL) relation. The PL relation has a physical basis (i.e. the PL relation is directly linked to the period–radius relation), and both the period and luminosity of the RRL can be objectively measured. In the mid-IR minimal extinction corrections are required ( $A_{[3.6]} \approx A_V/16$ , Indebetouw et al. 2005), and the dispersion of the relation in the infrared has been shown to be small compared to optical wavelengths (Marconi et al. 2015; Catelan et al. 2004). Through this decrease in dispersion we have found that the intrinsic width of the mid-IR PL for RRL is in fact *smaller* than for Cepheids – less than 0.05 mag compared to 0.10 mag (Neeley et al. 2015; Scowcroft et al. 2011). This translates to an uncertainty on an individual RRL of below 2% for RRL, compared to 4% for Cepheids at 3.6  $\mu$ m. Thus, for nearby systems RRL are the most precise standard candles.

Although observing RRL at mid-IR wavelengths dramatically reduces the effects of reddening and extinction, the consequences of this shift to longer wavelengths on other parameters in the empirical RRL PL relation are yet to be determined. The most important factor that must be considered is the effect of metallicity. Both theory and observation have demonstrated that the position of the horizontal branch in the optical colour–magnitude diagram is dependent on metallicity (e.g. Marconi et al. 2015; Catelan et al. 2004; Bono et al. 2003; Nemec et al. 1994). However, the size of the metallicity contribution in the infrared PL relation is yet to be settled in the literature, either from a theoretical or empirical standpoint.

The most in-depth study of the effect of metallicity on the mid-IR PL relation to date comes from Dambis et al. (2015), who used the ALLWISE data release (Wright et al. 2010; Cutri & et al. 2014) to examine possible changes in the RRL PL relation in globular clusters with different

metallicities. They found a moderate dependence of [W1] (approximately equivalent to *Spitzer* [3.6]) with [Fe/H] of  $\gamma_{W1} = 0.102 \text{ mag dex}^{-1}$ , slightly larger than their value for near-IR, and approximately half that of the optical dependence ( $\gamma_K = 0.088 \text{ mag dex}^{-1}$ ,  $\gamma_V = 0.232 \text{ mag dex}^{-1}$ ). The observational work of [Muraveva et al. \(2015\)](#) appears to confirm this result, favouring a low value of  $\gamma_K$  for Milky Way and LMC RRL. However, the empirical study of [Karczmarek et al. \(2015\)](#) considers near-IR observations of RRL in the Carina dwarf Spheroidal (dSph) galaxy, this time testing different PL relations with a range of metallicity coefficient. Their results favour a larger value for  $\gamma_K$  than [Dambis et al. \(2015\)](#), with average values of  $\gamma_K \approx 0.18 \text{ mag dex}^{-1}$ . This is consistent with the theoretical models by [Marconi et al. \(2015\)](#), who find that the metallicity dependence of the infrared PL relation is just as large as at optical wavelengths.

In this work we focus on the effects of metallicity on the RRL PL relation in the mid-IR. Several Galactic Globular Clusters are being observed as part of CRRP, but  $\omega$  Cen is unique in that it exhibits a measurable spread in metallicity, with the most recent results estimating  $0.8 \leq \Delta [\text{Fe}/\text{H}] \leq 1.4 \text{ dex}$  ([Villanova et al. 2014](#); [Marino et al. 2012](#); [Johnson & Pilachowski 2010](#)). This makes  $\omega$  Cen the ideal site for a metallicity study, as all the RRL can be considered to be at the same distance, leaving the metallicities of the individual stars as the only free parameter.  $\omega$  Cen has been used previously for such studies, ranging from empirical tests in the optical (e.g. [Olech et al. 2003](#); [Lee 1991](#)) and near-IR (e.g. [Cacciari et al. 2006](#); [Del Principe et al. 2006](#)), to semi-empirical tests using population synthesis techniques ([Tailo et al. 2016](#)). Our study is unique as it is the first study to use the RRL population of  $\omega$  Cen to empirically measure the metallicity effect on the mid-IR RRL PL relation.

The paper is set out as follows: Section 2 details the observations and data reduction. Section 3 presents the photometry of the  $\omega$  Cen RRL. Section 4 describes the mid-IR PL relations and Section 5 discusses the application of these to a distance measurement of  $\omega$  Cen. Section 6 examines the effects of metallicity on RRL magnitudes and distance estimates. Section 7 discusses the implications of this, and other systematic effects we consider in this work. In Section 8 we present our conclusions.

## 2 OBSERVATIONS & DATA REDUCTION

This work combines mid-IR observations from the Warm *Spitzer* mission ([Freedman et al. 2012a](#), PID 90002) with supporting near-IR observations from the FourStar instrument on the Baade-Magellan telescope at Las Campanas Observatory ([Persson et al. 2013](#)). Figure 1 shows a  $K_s$  FourStar image with the *Spitzer* fields outlined, the positions of known RRab plotted as circles, and the positions of known RRC as triangles.

### 2.1 Warm *Spitzer* Data

The Warm *Spitzer* observations for this work were taken as part of the CRRP. Three fields in  $\omega$  Cen were chosen; their positions and the positions of known  $\omega$  Cen RRLs are shown in Figure 1. To obtain optimal RRL light curves we

observed each field 12 times over approximately 16 hours, roughly corresponding to the period of the longest period RRL we expected in the field. The observations of all three fields were taken on 2013 May 10 and 2013 May 11. Each field was observed using the *Spitzer* InfraRed Array Camera (IRAC) ([Fazio et al. 2004](#)) with a 30 s frame time with a medium scale, and gaussian 5-point dither pattern to mitigate any image artefacts. Images were collected in both the 3.6 and 4.5  $\mu\text{m}$  channels. The elongated field shapes come from the design of IRAC; while the [3.6] channel is collecting on-target data, the [4.5] channel collects off target data “for free”, and vice versa. We chose to include these off-target fields to maximise the number of RRL in our final sample and to increase the legacy value of our data set to the community.

The science images were created using MOPEX ([Makovoz et al. 2006](#)), first running overlap correction on the corrected basic calibrated data frames (cBCDs) then mosaicking them at 0.6 arcsec pixel scale using the drizzle algorithm. Mosaicked location-correction images were created at the same time.

PSF photometry was performed using DAOPHOT and ALLFRAME ([Stetson 1987, 1994](#)). The PSF model was created for each field/filter combination using the first epoch data and was applied to every epoch. As the observations were taken temporally close together the effects of telescope rotation between epochs on the mosaicked PSF were minimal, so making a single good PSF model for each field/filter combination was much more efficient than creating one for every epoch.

Master star lists for ALLFRAME were created for each filter/field combination using a median mosaicked image created by MOPEX. We did not use the same single master star list for both filters as only a small proportion (1/3) of the [3.6] and [4.5] fields overlap each other. Instead we performed separate ALLFRAME reductions for each filter, and combined the results after the fact using DAOMATCH and DAOMASTER. Our mid-IR photometry is calibrated to the standard system set by [Reach et al. \(2005\)](#).

### 2.2 FourStar Data

$J$ ,  $H$  and  $K_s$  data were taken with the FourStar instrument on the Baade-Magellan telescope at Las Campanas Observatory ([Persson et al. 2013](#)) on the nights of 2013 June 25, 2013 June 27, and 2013 June 28. Four epochs were obtained each night in each filter for a total of 12 epochs. A mosaic of  $5 \times 3$  slightly overlapping pointings (tiles), each with FourStar’s native  $10.9 \times 10.9$  arcminute field of view, covered a  $50 \times 30$  arcminute field of view centred on  $\omega$  Cen. Each tile consists of a 5 point dither pattern with a 5.8 second exposure time. Stacked mosaics of the entire field were made as well as individual tiles using a customised pipeline for FourStar data. The purpose of the individual tiles is to provide photometry with better time resolution than the large mosaic.

PSF photometry of the tiles was performed using DAOPHOT and ALLFRAME ([Stetson 1987, 1994](#)). A PSF model was created for each epoch/tile/filter combination. A master star list for ALLFRAME was created from the final  $K_s$  mosaic and the multi-wavelength/epoch results were combined using DAOMATCH and DAOMASTER. Our final photometry is

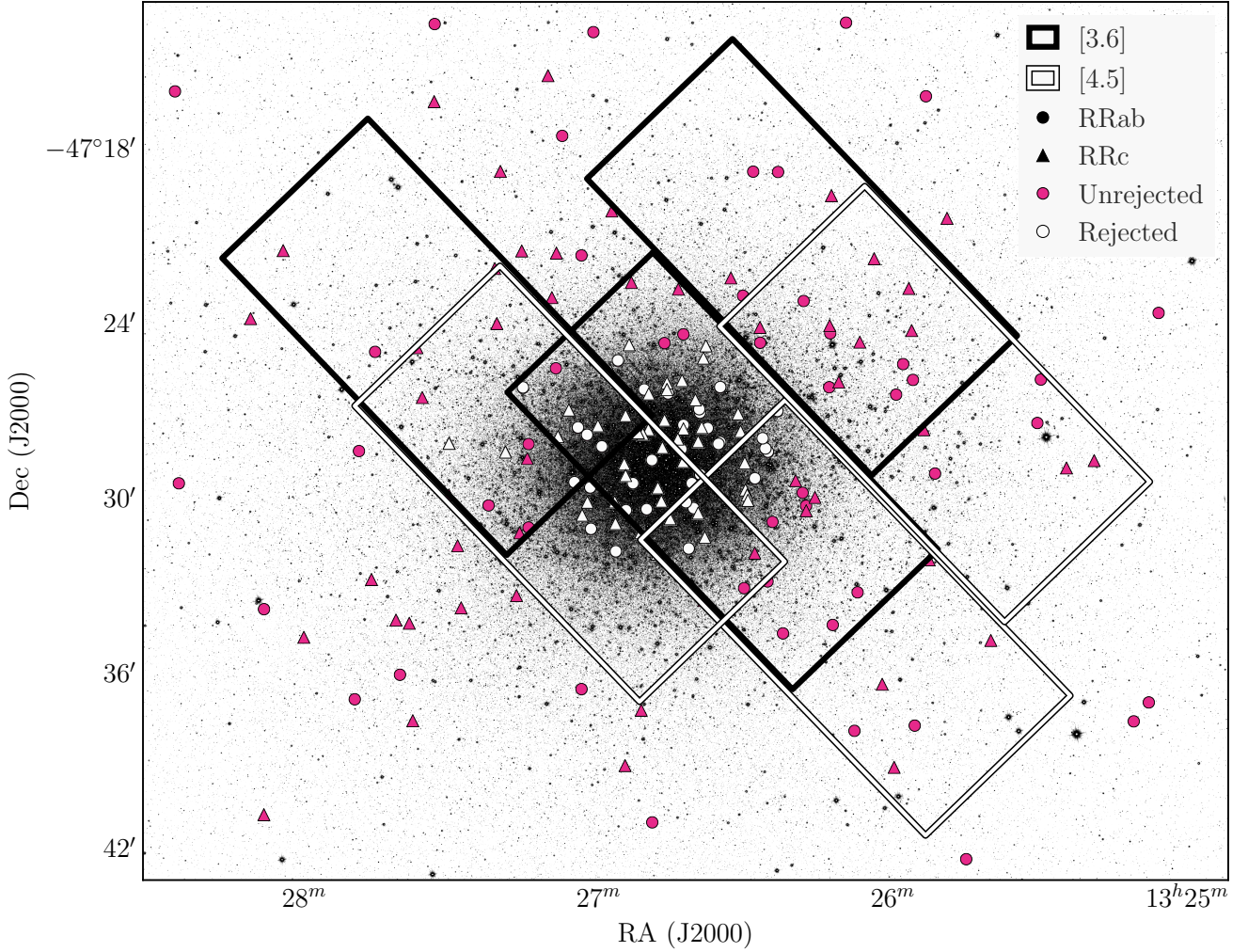


**Figure 1.** A  $K_s$ -band image of  $\omega$  Cen from the FourStar camera, overlaid with a catalog of RRL from Kaluzny et al. (2004) and footprints of the *Spitzer* IRAC fields. The circular points are RRab's and the triangular points are RRc's; we adopt this convention throughout the paper. The three black rectangle outlines are the IRAC field of view for each pointing in the 3.6  $\mu\text{m}$  channel, and the white rectangle outlines show the same for 4.5  $\mu\text{m}$ .

calibrated to the 2MASS standard system (Skrutskie et al. 2006).

### 2.3 Crowding

The primary limiting factor in the photometric precision is crowding. To assess crowding for individual RRLs, we compared the *Spitzer* images to the FourStar  $K_s$ -band image. The 0.159 arcsec/pixel resolution of the  $K_s$  band image compared to the 0.6 arcsec/pixel resolution of the IRAC images enabled us to more accurately determine which stars were significantly contaminated. RRL were determined to be contaminated if there were one or more resolved stars in the  $K$ -band image within a 3.6 arcsecond (6 IRAC pixels) radius of the RRL. 77 RRLs out of the original catalog of 192 (Kaluzny et al. 2004) were rejected due to crowding, another 13 were outside the FourStar mosaic field of view, and four more were found to be unusable due to contamination.

### 3 RESULTS

Our final photometry catalog, including magnitudes and uncertainties for  $JHK_s$ , [3.6], and [4.5], is presented in Table A1. **Note: this will not be an appendix in the final draft, we're just putting it there for now because it's huge.** The average magnitudes presented in Table A1 are flux averages, and the photometric uncertainties of the time series data are the error on the mean.

Our full, uncrowded RRL sample consists of 96 stars in  $J$  and  $H$ , 98 in  $K_s$ , 38 in [3.6], and 42 in [4.5]; the small number of stars in the IRAC bands compared to the FourStar bands is due to the smaller coverage of the IRAC pointings (see Figure 1). For the PL fitting, detailed Section 4, we use only the stars for which we have photometry in all five bandpasses, ensuring that the same range of periods and metallicities are sampled for each wavelength. This helps to reduce any biases that may be introduced by non-uniform sampling in the distance moduli fits in Section 5. Our final



**Table 1.** Empirical mid-IR RRL period-luminosity relation coefficients (Neeley et al. 2015), for relations of the form  $M = a + b \times (\log(P) + P_0)$  with intrinsic dispersion  $\sigma$ . These relations are derived from RRL in the globular cluster M4.

Band	Mode	$a$	$b$	$P_0$	$\sigma$
[3.6]	RRab	-0.558	-2.370	0.260	0.040
	RRc	-0.192	-2.658	0.550	0.079
[4.5]	RRab	-0.593	-2.355	0.260	0.045
	RRc	-0.240	-2.979	0.550	0.057

**Table 2.** Theoretical near-IR RRL period-luminosity relation coefficients (Marconi et al. 2015), for relations of the form  $M = a + b \times \log P + c \times [\text{Fe}/\text{H}]$  with intrinsic dispersion  $\sigma$ .

Band	Mode	$a$	$b$	$c$	$\sigma$
$J$	RRab	-0.510	-1.980	0.170	0.060
	RRc	-1.070	-2.460	0.150	0.040
$H$	RRab	-0.760	-2.240	0.190	0.040
	RRc	-1.310	-2.700	0.160	0.020
$K_s$	RRab	-0.820	-2.270	0.180	0.030
	RRc	-1.370	-2.720	0.150	0.020

RRL sample consists of 24 stars, with 12 in each pulsation mode.

#### 4 PERIOD-LUMINOSITY RELATIONS

We fit PL relations using the theoretical near-infrared PL relation parameters presented in Marconi et al. (2015) for the  $JHK_s$  bands, and the empirical PL relation parameters derived from photometry of RRLs in the globular cluster M4 (NGC 6121) from Neeley et al. (2015) for the IRAC bands. With the use of preexisting PL relation coefficients, the distance modulus becomes the only free parameter in our fit. We fit all distance moduli using an unweighted least-squares method, and fit the distance modulus to each pulsation mode in each wavelength separately. We also refine the fit by sigma-clipping the residuals of the [3.6] fit at a  $2\sigma$  level, resulting in the rejection of two more stars.

For the mid-IR we use the PL relations from Neeley et al. (2015), as described in Table 1. These relations take the form

$$M = a + b \times (\log(P) + P_0) \quad (1)$$

where  $a$  and  $b$  are empirically derived coefficients and  $P_0$  is the absolute value of the logarithm of the mean period of the M4 RRL sample. We calculate the absolute PL zero-points adopting Neeley et al.'s M4 distance modulus of  $\mu = 11.399$  mag.

The  $JHK_s$  RRL PL relations are described in Table 2. The relations take the form

$$M = a + b \times \log P + c \times [\text{Fe}/\text{H}] \quad (2)$$

where  $a$ ,  $b$ , and  $c$  are theoretically derived coefficients.

The theoretical PL relations for the near-IR have a metallicity-dependent term; however, we do not have known metallicities for all RRL in our sample. We therefore use the average  $[\text{Fe}/\text{H}]$  of the RRLs for which there are known

metallicities. Using spectroscopic metallicities from Sollima et al. (2006), we obtain an average  $[\text{Fe}/\text{H}]$  of  $-1.677$ .

#### 5 DISTANCE MODULI

We combine the uncorrected distance moduli from each bandpass to obtain a mean reddening value and reddening-corrected distance modulus. We fit the near-infrared reddening law from Cardelli et al. (1989) to the  $JHK_s$  data and the mid-infrared law from Indebetouw et al. (2005) to [3.6] and [4.5] simultaneously, assuming a ratio of total to selective absorption  $R_V = 3.1$ . The resulting fit is shown in Figure 4. We derive a true mean dereddened distance modulus of  $\langle \mu_0 \rangle = 13.789 \pm 0.018$  with  $E(B - V) = 0.084 \pm 0.030$  using the weighted mean RRab + RRc distances. The individual uncorrected distance moduli  $\mu$ , corrected distance moduli  $\mu_0$ , and PL residuals are shown in Table 3.

It is apparent from Figure 4 that there are large discrepancies in the distance moduli in [3.6] and [4.5] for the two pulsation modes; these discrepancies contribute to the relatively low  $E(B - V)$  value and high dereddened distance modulus compared to previously determined values (e.g. Lub 2002; Del Principe et al. 2006). If we remove the RRc's and fit the extinction curve only to the RRab's, as shown in Figure 5, we obtain a better fit of all points to the extinction curve than when we use the mean. From these distance moduli we derive a true dereddened distance modulus of  $\langle \mu_0 \rangle = 13.743 \pm 0.026$  with  $E(B - V) = 0.138 \pm 0.044$ , both of which are closer to accepted values than the values derived from the weighted mean distance moduli. All individual corrected distance moduli from this fit are shown in Table 4.

Given the large errors in the [4.5] distances, we also fit the extinction curve to the  $JHK_s$  and [3.6] distances only, excluding [4.5] entirely; this was found to have a negligible effect on the final distance modulus and reddening for both the mean and RRab-only measurements.

#### 6 METALLICITY

Theoretical models suggest that the metallicity dependence of the RRL PL relation should decrease monotonically from the optical to the near-infrared (Bono et al. 2001; Catelan et al. 2004). Observational evidence corroborates this; previous investigations performed on WISE data suggest no obvious metallicity dependence in the mid-IR PL relations (Madore et al. 2013).

$\omega$  Cen is ideal for examining the RRL period-luminosity-metallicity relation, because it is known to have a large spread in metallicity ( $0.8 \leq \Delta [\text{Fe}/\text{H}] \leq 1.4$  dex Villanova et al. 2014; Marino et al. 2012; Johnson & Pilachowski 2010). A metallicity spread this wide is not found in any other Galactic globular cluster. One of the advantages of using globular clusters to calibrate PL coefficients is that all stars in a cluster can be considered to be at the same distance from Earth. The dispersion in the PL relation is a combination of the a) the intrinsic dispersion of the PL relation, b) the photometric uncertainties, and c) dispersion induced by other complicating factors such as the spread

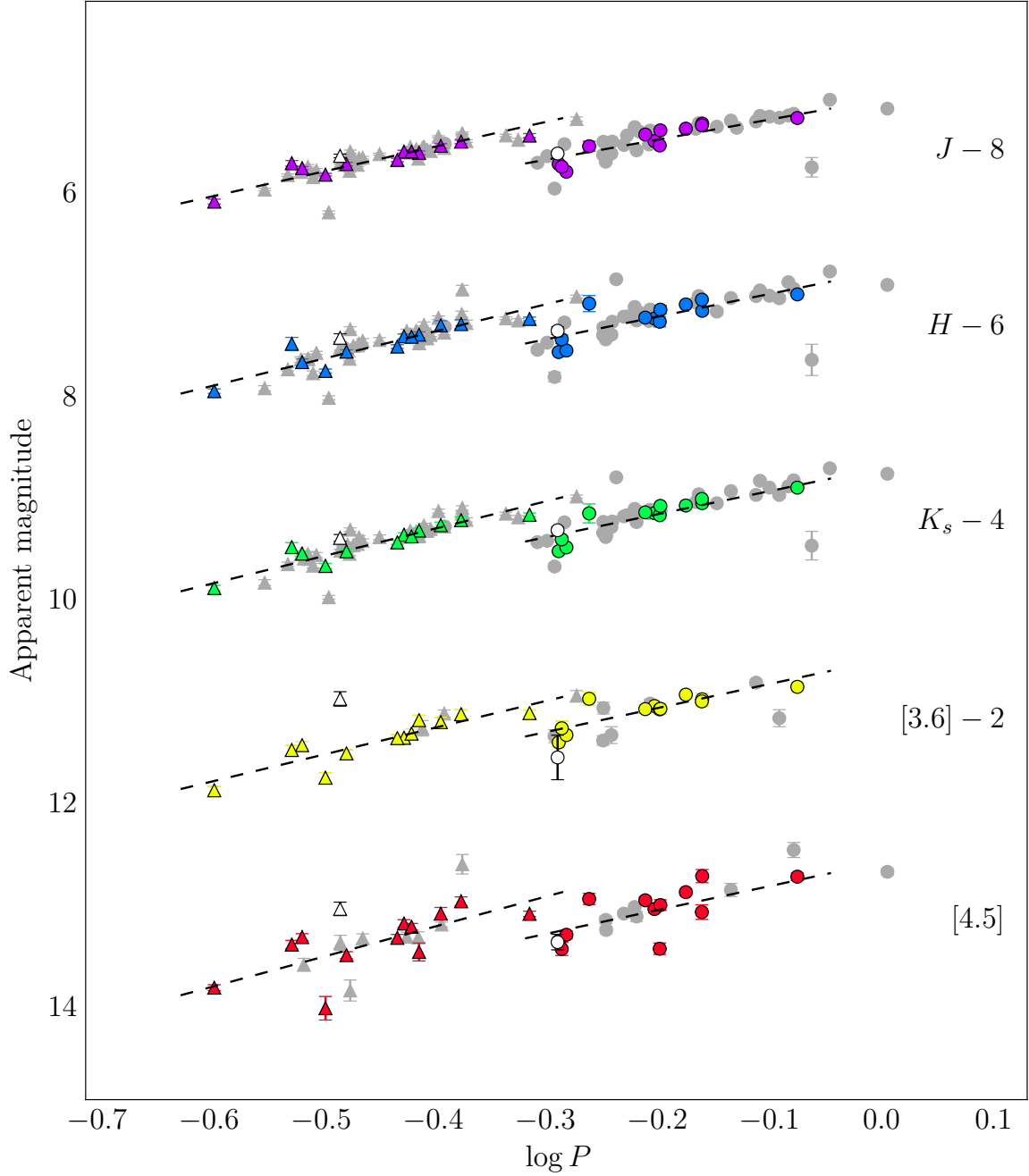


**Figure 2.** PL relations for  $JHK_s$ ,  $[3.6]$ , and  $[4.5]$  photometry assuming  $[\text{Fe}/\text{H}] = -1.677$ . Here circles represent RRab stars and triangles represent RRc's. Coloured points are the final consistent sample with photometry in all 5 wavebands and grey points are stars that did not appear in all bands. The unfilled points are stars rejected from the final sample based on  $2\sigma$  clipping of the PL residuals in  $[3.6]$ .

in metallicity. Since we have measured the intrinsic dispersion of the RRL PL in  $[3.6]$  and  $[4.5]$  from the cluster M4 (Neeley et al. 2015) and our photometric uncertainties are well understood, we can isolate the remaining scatter due to astrophysical sources such as metallicity.

We know from mid-IR spectra that a significant CO feature sits within the IRAC  $[4.5]$  filter. In the case of Cepheids, ? have shown that this has a significant effect on the  $[4.5]$

magnitudes, and is metallicity dependent. However, this effect decreases with increasing temperatures, turning off completely above 6000 K where all the CO has been destroyed (?). As even the coolest RRL have temperatures over 6000 K (Iben 1971), we expect to see no such CO absorption in the  $[4.5]$  PL relation, nor do we expect any other metallicity effects. However, we can directly and empirically test this prediction.

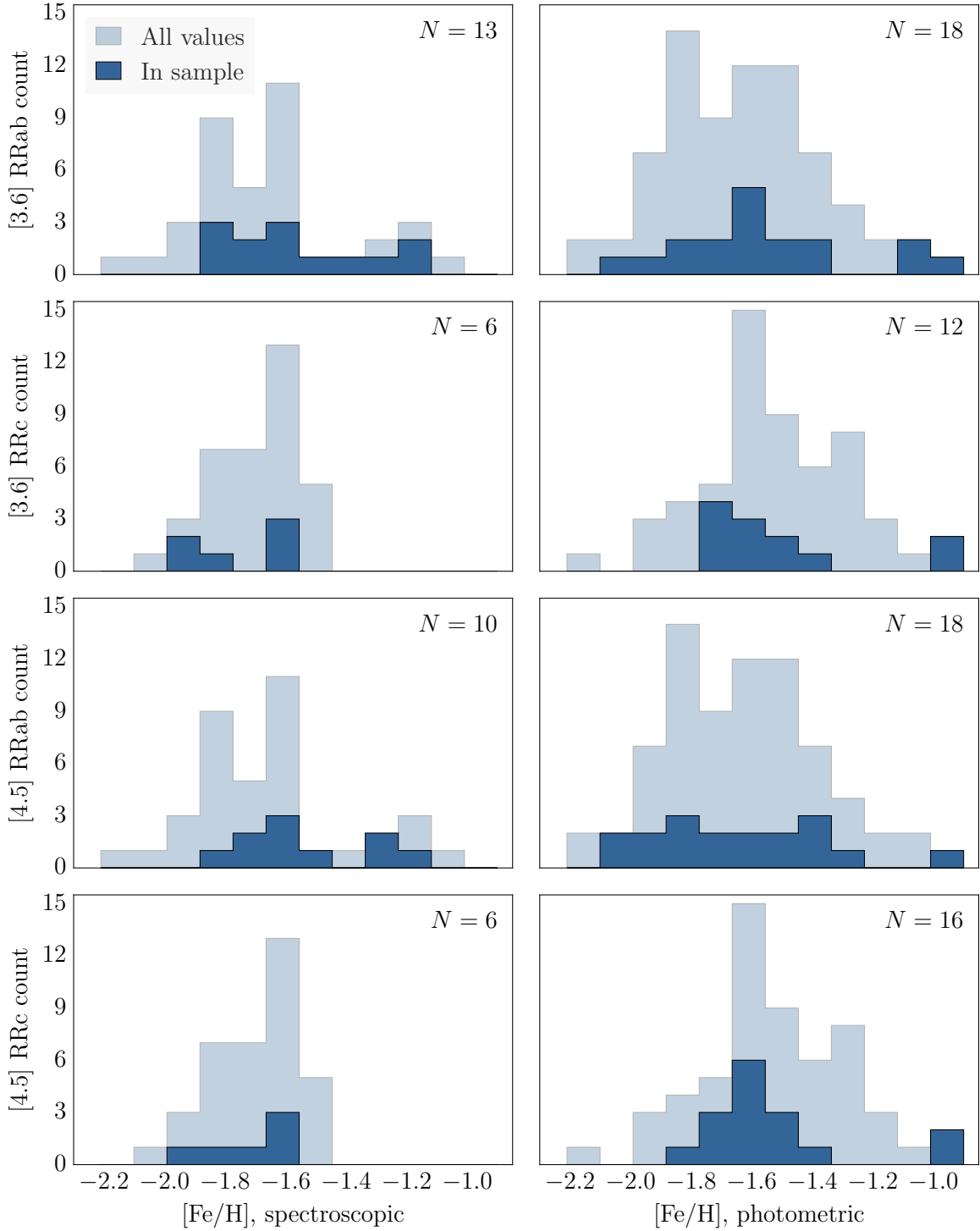


**Figure 3.** Histograms of spectroscopic (Sollima et al. 2006, right column) and photometric (Rey et al. 2000, left column) [Fe/H] values for RRab (top row) and RRc (bottom row). The light blue histograms represent all known metallicity values for each type, and the dark blue are the metallicity values in our final RRL sample. The number  $N$  at the top right corner of each subplot is the number of stars in our final sample that have known metallicity values for the given type and metallicity catalog.

**Table 3.** Uncorrected distance moduli  $\mu$ , corrected distance moduli  $\mu_0$ , and the PL dispersion  $\sigma$ . The corrected distance moduli  $\mu_0$  are equal to  $\mu - A_\lambda A_V$ , where  $A_V$  is derived from fitting the reddening laws to the mean distance moduli.

Band	$\mu$ , R Rab	$\mu$ , R Rc	$\mu$ , mean	$\mu_0$ , R Rab	$\mu_0$ , R Rc	$\mu_0$ , mean	$\sigma_{\text{PL}}$ , R Rab	$\sigma_{\text{PL}}$ , R Rc
$J$	$13.865 \pm 0.023$	$13.866 \pm 0.019$	$13.865 \pm 0.015$	$13.788 \pm 0.036$	$13.790 \pm 0.033$	$13.789 \pm 0.031$	0.127	0.082
$H$	$13.821 \pm 0.032$	$13.844 \pm 0.026$	$13.832 \pm 0.021$	$13.773 \pm 0.037$	$13.796 \pm 0.031$	$13.784 \pm 0.027$	0.170	0.107
$K_s$	$13.816 \pm 0.025$	$13.831 \pm 0.021$	$13.824 \pm 0.016$	$13.786 \pm 0.027$	$13.801 \pm 0.024$	$13.794 \pm 0.020$	0.147	0.089
[3.6]	$13.750 \pm 0.026$	$13.838 \pm 0.031$	$13.794 \pm 0.020$	$13.733 \pm 0.027$	$13.821 \pm 0.031$	$13.777 \pm 0.021$	0.124	0.096
[4.5]	$13.771 \pm 0.052$	$13.890 \pm 0.061$	$13.830 \pm 0.040$	$13.756 \pm 0.052$	$13.875 \pm 0.061$	$13.816 \pm 0.040$	0.154	0.219

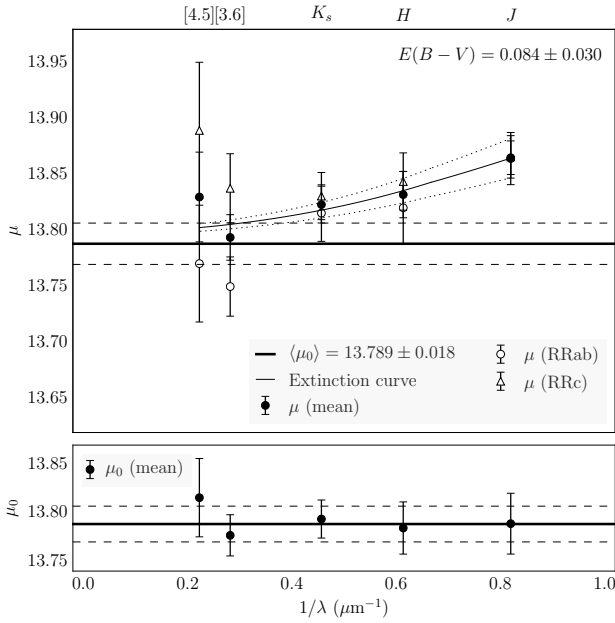


**Figure 4.** Top: Uncorrected distance moduli for the final sample of  $JHK_s$ , [3.6], and [4.5] photometry. Filled circles are the mean distance moduli using both R Rab and R Rc stars, open circles are the distance moduli using only R Rab stars, and open triangles are distance moduli using only R Rc stars. Here the NIR and MIR reddening laws are fit to the mean distance moduli. The solid and dashed horizontal lines are the mean corrected distance modulus and its  $1\sigma$  errors respectively. Bottom: reddening-corrected distance moduli and mean corrected distance modulus. Errors on the corrected distance moduli are the quadrature sum of the uncorrected distance moduli errors and the reddening error at the requisite wavelength.

**Table 4.** Corrected distance moduli  $\mu_0$  using the  $A_V$  value derived from fitting the reddening laws to only the R Rab distance moduli.

Band	$\mu_0$ , R Rab	$\mu_0$ , R Rc	$\mu_0$ , mean
$J$	$13.739 \pm 0.047$	$13.741 \pm 0.045$	$13.740 \pm 0.043$
$H$	$13.742 \pm 0.041$	$13.766 \pm 0.036$	$13.754 \pm 0.033$
$K_s$	$13.767 \pm 0.030$	$13.782 \pm 0.026$	$13.775 \pm 0.023$
[3.6]	$13.722 \pm 0.028$	$13.810 \pm 0.032$	$13.766 \pm 0.022$
[4.5]	$13.747 \pm 0.053$	$13.866 \pm 0.061$	$13.806 \pm 0.041$

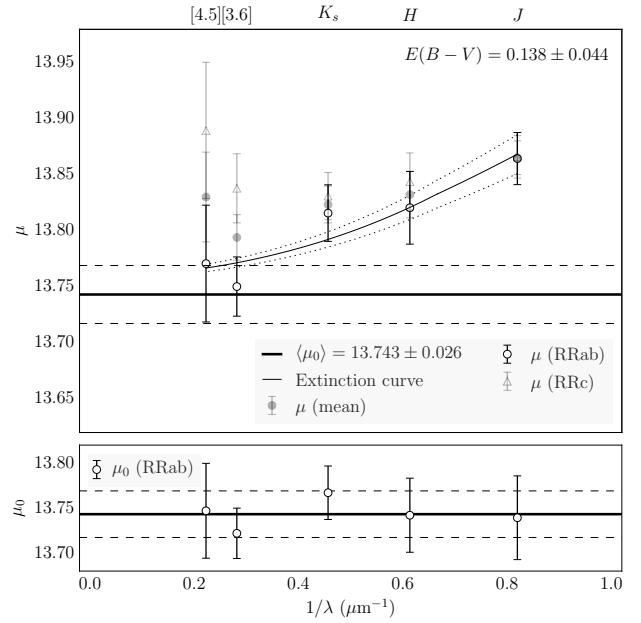


**Figure 5.** Same as Figure 4, with the reddening laws fit to the R Rab distances only instead of the mean.

### 6.1 Metallicity Contribution to the Overall Dispersion

We can place an upper limit on the contribution of metallicity to the  $\omega$  Cen PL dispersion using the known variances of the observed distribution of  $\omega$  Cen PL residuals  $\sigma_{\text{observed}}^2$ , the intrinsic PL width  $\sigma_{\text{intrinsic}}^2$ , and the scatter induced by photometric error  $\sigma_{\text{phot}}^2$ . The scatter contributed by metallicity can therefore be constrained as follows:

$$\sigma_{[\text{Fe}/\text{H}]} \leq \sqrt{\sigma_{\text{observed}}^2 - \sigma_{\text{intrinsic}}^2 - \sigma_{\text{phot}}^2} \quad (3)$$

The calculated  $\sigma_{[\text{Fe}/\text{H}]}$  values for all IRAC PL relations are shown in Table 5, along with  $\sigma_{\text{observed}}$  and the other scatter components.

We use these estimates of  $\sigma_{[\text{Fe}/\text{H}]}$  to assess the  $\gamma$  parameter for  $\omega$  Cen, where

$$\gamma = \frac{\Delta \text{mag}}{\Delta [\text{Fe}/\text{H}]} \text{ mag dex}^{-1}, \quad (4)$$

similar to  $\gamma$  used to quantify the effect of metallicity on the zero-point of the Cepheid PL relation (Kennicutt et al. 1998; Scowcroft et al. 2009). Here we calculate  $\gamma$  in units of  $\text{mag dex}^{-1}$  by dividing the standard deviation of the metallicity

**Table 5.** The standard deviation of the observed spread of the PL residuals  $\sigma_{\text{observed}}$  ( $\sigma_{\text{PL}}$  in Table 3) and its components:  $\sigma_{\text{intrinsic}}$  ( $\sigma$  in Table 1),  $\sigma_{\text{phot}}$ , and  $\sigma_{[\text{Fe}/\text{H}]}$  for all IRAC PL relations.

Band	Mode	$\sigma_{\text{observed}}$	$\sigma_{\text{intrinsic}}$	$\sigma_{\text{phot}}$	$\sigma_{[\text{Fe}/\text{H}]}$
<i>J</i>	RRab	0.127	0.060	0.018	0.111
	RRc	0.082	0.040	0.015	0.070
<i>H</i>	RRab	0.170	0.040	0.028	0.163
	RRc	0.107	0.020	0.024	0.102
<i>K<sub>s</sub></i>	RRab	0.147	0.030	0.023	0.142
	RRc	0.089	0.020	0.021	0.084
[3.6]	RRab	0.124	0.040	0.052	0.106
	RRc	0.096	0.079	0.044	0.034
[4.5]	RRab	0.154	0.045	0.046	0.140
	RRc	0.219	0.057	0.054	0.205

**Table 6.** Metallicity standard deviations and  $\gamma$  values.

Band	Mode	$\sigma_{\text{spect}}$	$\sigma_{\text{phot}}$	$\gamma_{\text{spect}}$	$\gamma_{\text{phot}}$
<i>J</i>	RRab	0.215	0.262	0.515	0.423
	RRc	0.132	0.245	0.529	0.285
<i>H</i>	RRab	0.215	0.260	0.760	0.627
	RRc	0.132	0.245	0.773	0.416
<i>K<sub>s</sub></i>	RRab	0.215	0.258	0.659	0.549
	RRc	0.132	0.242	0.636	0.347
[3.6]	RRab	0.232	0.275	0.455	0.385
	RRc	0.145	0.266	0.237	0.129
[4.5]	RRab	0.215	0.285	0.653	0.492
	RRc	0.107	0.244	1.904	0.837

component of the PL scatter by the standard deviation of the metallicity distribution for both (Sollima et al. 2006) and photometric (Rey et al. 2000) metallicities; the results for each PL are shown in Table 6. We use all available metallicity values for each pulsation mode when taking the standard deviation, as we do not have metallicity values for all the stars in our samples, although the metallicity values we do have trace the overall metallicity distributions fairly well (see Figure 3).

For [3.6] we find  $\gamma \leq 0.455 \text{ mag dex}^{-1}$  for RRab's, and  $\gamma \leq 0.237 \text{ mag dex}^{-1}$  for RRc's.

## 6.2 PL Residuals and Individual Metallicities

$\omega$  Cen provides a second approach to testing for a metallicity effect on the RRL PL relation. The cluster is extremely well studied and many of its RRL have spectroscopic or photometric metallicities in the literature (e.g. Sollima et al. 2006; Rey et al. 2000).

Theory predicts a linear metallicity term in the PLZ relation for the near-IR,  $c \times [\text{Fe}/\text{H}]$ . We thus fit a relation of the form

$$\Delta\text{mag} = \gamma \times [\text{Fe}/\text{H}] + d \quad (5)$$

to the [3.6] and [4.5] PL residuals and metallicity values for stars with known individual metallicity values, as shown in Figure 6. The scatter in the [3.6] and [4.5] PL relations is higher for  $\omega$  Cen than it is for M4 (Neeley et al. 2015; Braga et al. 2015); however, when we examine  $[\text{Fe}/\text{H}]$  vs. the residuals of each PL relation,  $\gamma$  is within  $1\sigma$  of zero

for all fits, indicating that there is no significant metallicity dependence in the PL residuals, consistent with predictions.

More accurate metallicities will be required to constrain any potential effect further.

## 7 DISCUSSION

While we find high upper bounds on the contribution of metallicity to the PL scatter in the IRAC passbands, particularly [4.5], it is unlikely that this scatter is due to metallicity alone. Gratton et al. (1986) and Lee (1991) demonstrate that RRL luminosity is dependent on the horizontal branch morphology as well as metallicity; it is also well known that  $\omega$  Cen contains RRLs in multiple evolutionary states (Sollima et al. 2008; Navarrete et al. 2015).

Results from the *GAIA* mission (Lindegren & Perryman 1996) are expected to improve the overall characterisation of the RRL PL relation dramatically. Trigonometric parallaxes and spectrophotometric metallicities of Galactic RRLs from *GAIA* will increase the number of calibrators for the absolute RRL PL relations by an order of magnitude (Liu et al. 2012, overview paper). **something about omega cen parallaxes and metallicities too**

We also anticipate that the NIRCcam instrument on *JWST* (Burriesci 2005; Gardner et al. 2006) will provide substantial improvements over IRAC for investigations of this nature. The NIRCcam filters F356W and F444W will provide data in passbands comparable to IRAC's [3.6] and [4.5] at an order of magnitude higher resolution (0.065 arc-sec/pixel), which will significantly decrease photometric error due to crowding and therefore allow us to obtain data for all known RRLs in  $\omega$  Cen.

## 8 CONCLUSIONS

We derive a true mean dereddened distance modulus for  $\omega$  Cen of  $\langle\mu_0\rangle = 13.739 \pm 0.024$  with reddening  $E(B - V) = 0.110 \pm 0.042$  using distance moduli derived from RRab PL relations in *JHK<sub>s</sub>*, [3.6], and [4.5]. Using the mean of RRab and RRc distance moduli in the same passbands, we derive a true mean dereddened distance modulus of  $\langle\mu_0\rangle = 13.781 \pm 0.018$  with reddening  $E(B - V) = 0.066 \pm 0.030$ . The RRab results are closer to literature values.

We also constrain the contribution of metallicity, quantified as  $\gamma = \Delta\text{mag}/\Delta[\text{Fe}/\text{H}]$ , to the scatter of the  $\omega$  Cen PL relations by subtracting the variances of the intrinsic scatter and photometric error from the observed PL variance and taking the square root of the result, and dividing that by the standard deviation of the distribution of metallicity values. We also measure  $\gamma$  directly using the slope of the linear fit to the PL residuals vs.  $[\text{Fe}/\text{H}]$ .

## ACKNOWLEDGEMENTS

We thank Eric Persson for his many contributions to this project.

This work is based on observations made with the Spitzer Space Telescope, which is operated by the Jet Propulsion Laboratory, California Institute of Technology



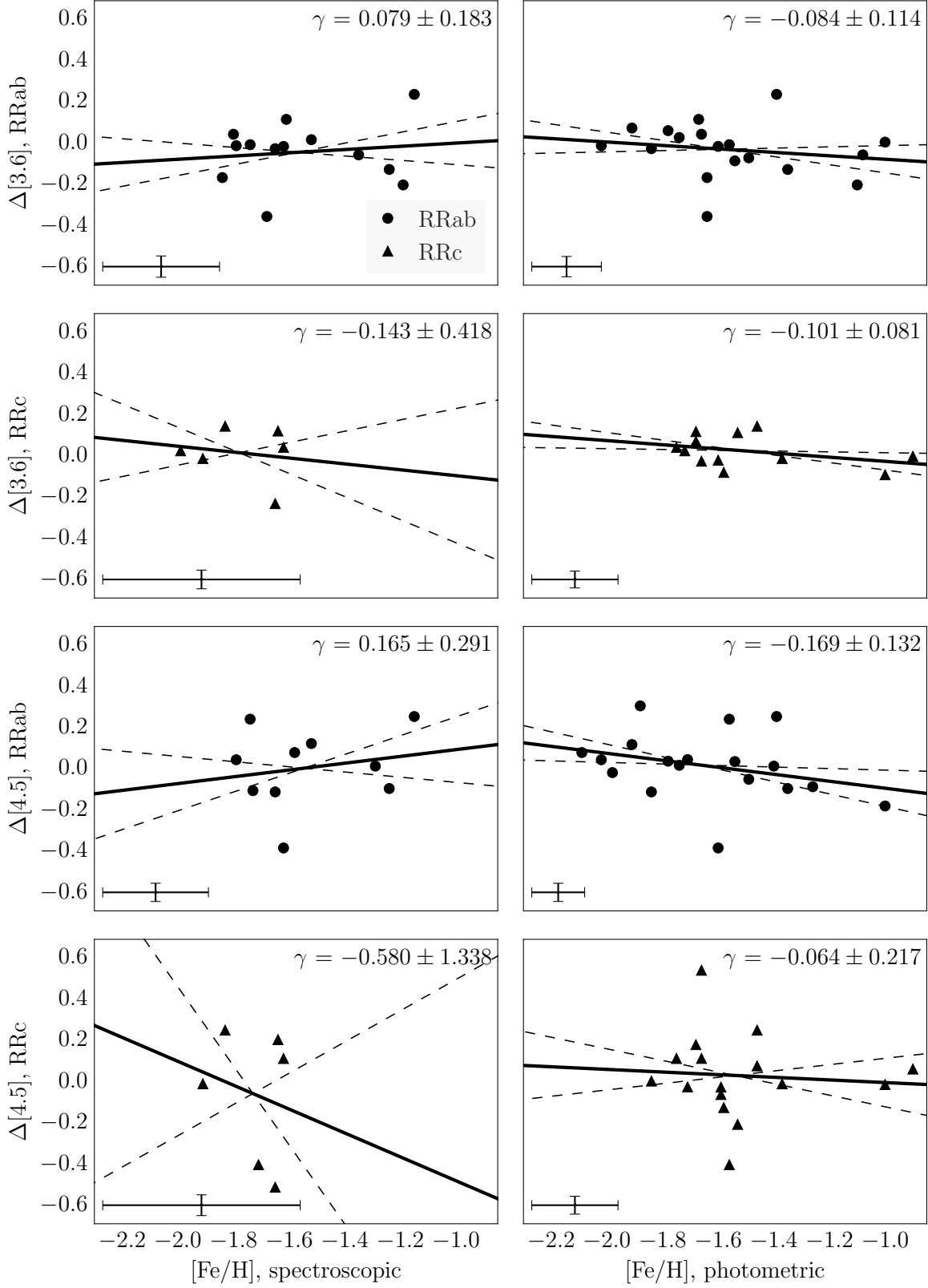


**Figure 6.** Photometric (Rey et al. 2000) and spectroscopic (Sollima et al. 2006) [Fe/H] values vs. period-luminosity residuals for RRab and RRc in [3.6] and [4.5]. Solid lines are the line of best fit with slope  $\gamma$ , and dashed lines are the  $1\sigma$  confidence intervals. The  $\gamma$  parameter from equation 4 in the top right corner of each subplot. All  $\gamma$  values are consistent with zero.

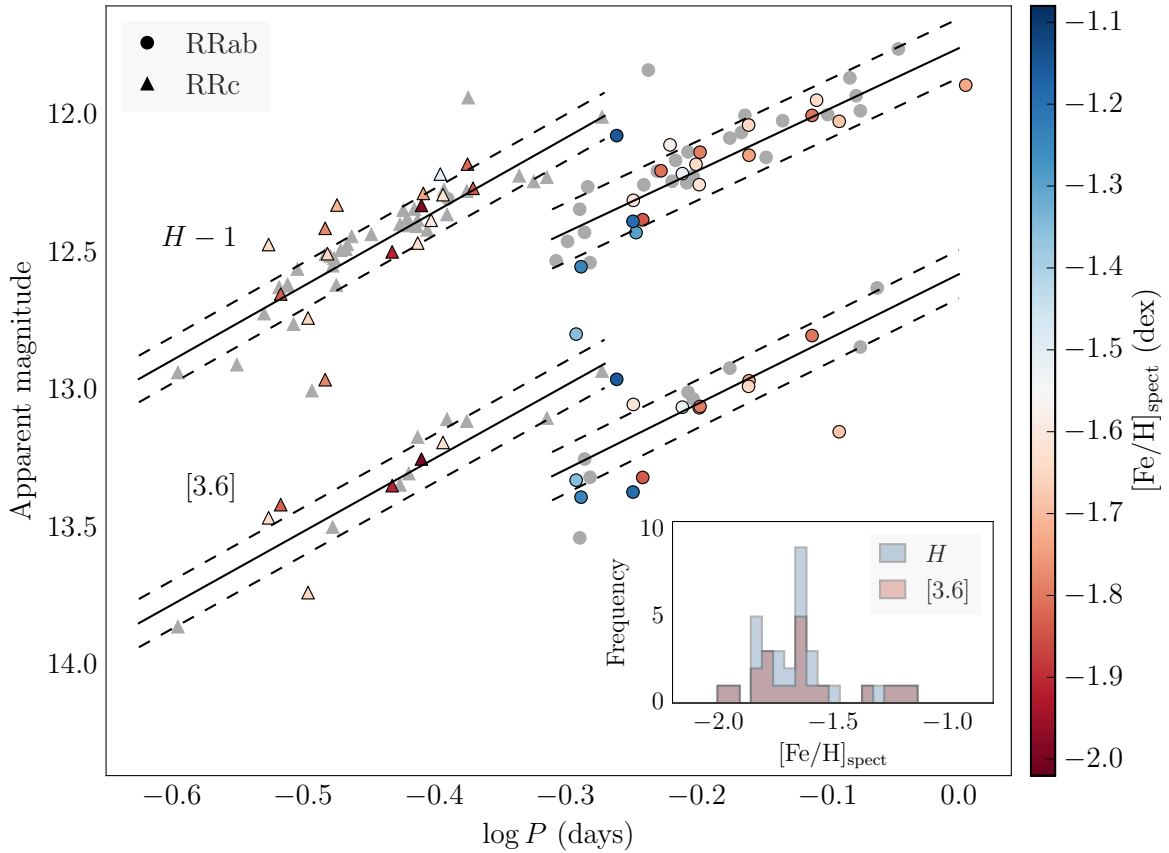


**Figure 7.** The  $H$ -band PL relation with fundamentalised RRc periods, with colour indicating spectroscopic (Sollima et al. 2006, top) and photometric (Rey et al. 2000, bottom) metallicity values. Grey points have no known metallicity values.

under a contract with NASA. Support for this work was provided by NASA through an award issued by JPL/Caltech.

This work was also supported in part by the Claremont-Carnegie Astrophysics Research Program.

This publication makes use of data products from the Two Micron All Sky Survey, which is a joint project of the University of Massachusetts and the Infrared Processing and Analysis Center/California Institute of Technology, funded by the National Aeronautics and Space Administration and the National Science Foundation.

This research has made use of the NASA/IPAC Extragalactic Database (NED), which is operated by the Jet Propulsion Laboratory, California Institute of Technology, under contract with the National Aeronautics and Space Administration.

## REFERENCES

- Aaronson M., Mould J., 1986, *ApJ*, **303**, 1
- Bono G., Caputo F., Castellani V., Marconi M., Storm J., 2001, *MNRAS*, **326**, 1183
- Bono G., Caputo F., Castellani V., Marconi M., Storm J., Degl’Innocenti S., 2003, *MNRAS*, **344**, 1097
- Braga V. F., et al., 2015, *ApJ*, **799**, 165
- Burriesci L. G., 2005, in Heaney J. B., Burriesci L. G., eds, Society of Photo-Optical Instrumentation Engineers (SPIE) Conference Series Vol. 5904, Cryogenic Optical Systems and Instruments XI. pp 21–29, [doi:10.1117/12.613596](https://doi.org/10.1117/12.613596)
- Cacciari C., Sollima A., Ferraro F. R., 2006, *Mem. Soc. Astron. Italiana*, **77**, 245
- Cardelli J. A., Clayton G. C., Mathis J. S., 1989, *ApJ*, **345**, 245
- Catelan M., Pritzl B. J., Smith H. A., 2004, *ApJS*, **154**, 633
- Cutri R. M., et al. 2014, VizieR Online Data Catalog, **2328**
- Dambis A. K., Berdnikov L. N., Kniazev A. Y., Kravtsov V. V., Rastorguev A. S., Sefako R., Vozyakova O. V., Zabolotskikh M. V., 2015, *Publication of Korean Astronomical Society*, **30**, 183
- Del Principe M., et al., 2006, *ApJ*, **652**, 362
- Efstathiou G., 2014, *MNRAS*, **440**, 1138
- Fazio G. G., et al., 2004, *ApJS*, **154**, 10
- Freedman W. L., et al., 2011, *AJ*, **142**, 192
- Freedman W., et al., 2012a, The Carnegie RR Lyrae Program, Spitzer Proposal
- Freedman W. L., Madore B. F., Scowcroft V., Burns C., Monson A., Persson S. E., Seibert M., Rigby J., 2012b, *ApJ*, **758**, 24
- Gardner J. P., et al., 2006, *Space Sci. Rev.*, **123**, 485
- Gratton R. G., Tornambe A., Ortolani S., 1986, *A&A*, **169**, 111
- Iben Jr. I., 1971, *PASP*, **83**, 697
- Indebetouw R., et al., 2005, *ApJ*, **619**, 931
- Johnson C. I., Pilachowski C. A., 2010, *ApJ*, **722**, 1373
- Kaluzny J., Olech A., Thompson I. B., Pych W., Krzemiński W., Schwarzenberg-Czerny A., 2004, *A&A*, **424**, 1101
- Karczmarek P., et al., 2015, *AJ*, **150**, 90
- Kennicutt Jr. R. C., et al., 1998, *ApJ*, **498**, 181

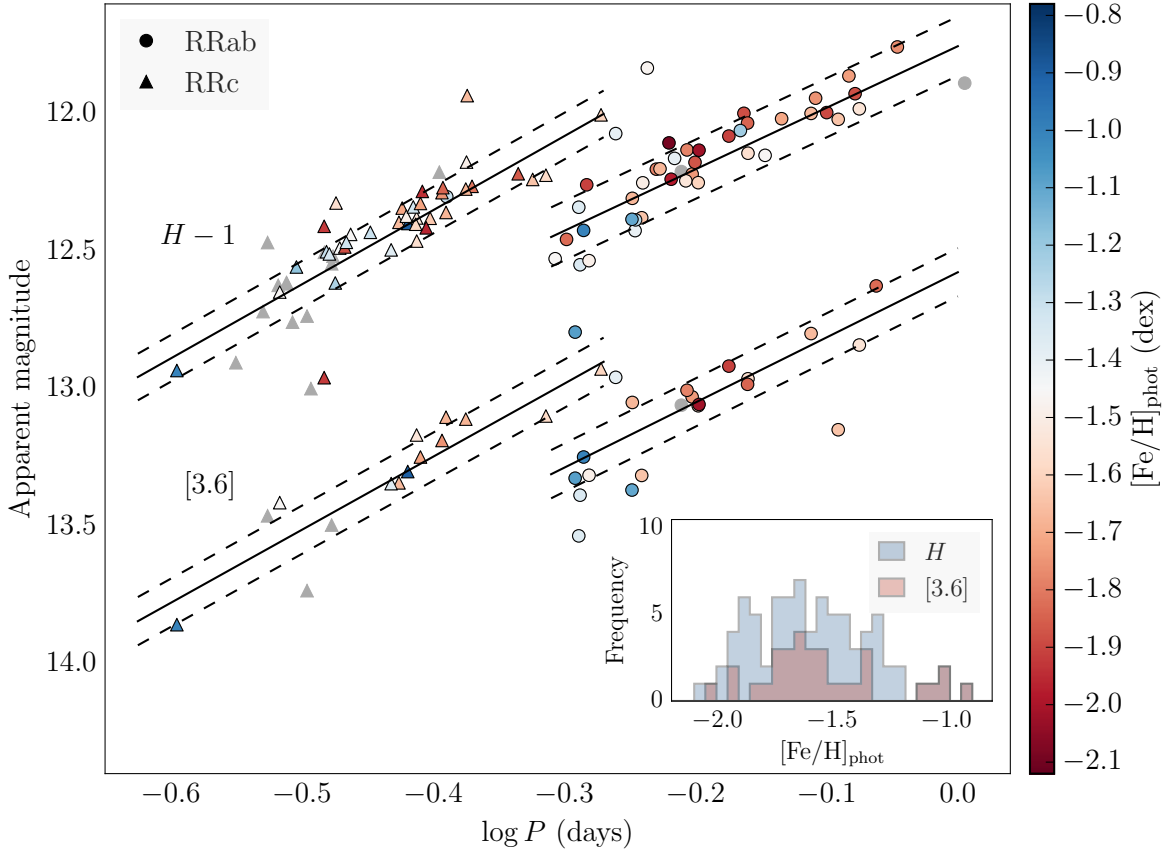


**Figure 8.** The  $H$ -band PL relation with fundamentalised RRC periods, with colour indicating spectroscopic (Sollima et al. 2006, top) and photometric (Rey et al. 2000, bottom) metallicity values. Grey points have no known metallicity values.

- Lee Y.-W., 1991, *ApJ*, **373**, L43
- Lindgren L., Perryman M. A. C., 1996, *A&AS*, **116**, 579
- Liu C., Bailer-Jones C. A. L., Sordo R., Vallenari A., Borrachero R., Luri X., Sartoretti P., 2012, *MNRAS*, **426**, 2463
- Longmore A. J., Fernley J. A., Jameson R. F., 1986, *MNRAS*, **220**, 279
- Lub J., 2002, in van Leeuwen F., Hughes J. D., Piotto G., eds, *Astronomical Society of the Pacific Conference Series Vol. 265, Omega Centauri, A Unique Window into Astrophysics*. p. 95
- Madore B. F., et al., 2013, *ApJ*, **776**, 135
- Makovoz D., Roby T., Khan I., Booth H., 2006, in *Society of Photo-Optical Instrumentation Engineers (SPIE) Conference Series*. p. 62740C, doi:10.1117/12.672536
- Marconi M., et al., 2015, *ApJ*, **808**, 50
- Marino A. F., et al., 2012, *ApJ*, **746**, 14
- Muraveva T., et al., 2015, *ApJ*, **807**, 127
- Navarrete C., et al., 2015, *A&A*, **577**, A99
- Neeley J. R., et al., 2015, *ApJ*, **808**, 11
- Nemec J. M., Nemec A. F. L., Lutz T. E., 1994, *AJ*, **108**, 222
- Olech A., Kaluzny J., Thompson I. B., Schwarzenberg-Czerny A., 2003, *MNRAS*, **345**, 86
- Persson S. E., et al., 2013, *PASP*, **125**, 654
- Reach W. T., et al., 2005, *PASP*, **117**, 978
- Rey S.-C., Lee Y.-W., Joo J.-M., Walker A., Baird S., 2000, *AJ*, **119**, 1824
- Riess A. G., et al., 2011, *ApJ*, **730**, 119
- Rigault M., et al., 2015, *ApJ*, **802**, 20
- Scowcroft V., Bersier D., Mould J. R., Wood P. R., 2009, *MNRAS*, **396**, 1287
- Scowcroft V., Freedman W. L., Madore B. F., Monson A. J., Persson S. E., Seibert M., Rigby J. R., Sturch L., 2011, *ApJ*, **743**, 76
- Skrutskie M. F., et al., 2006, *AJ*, **131**, 1163
- Sollima A., Borissova J., Catelan M., Smith H. A., Minniti D., Cacciari C., Ferraro F. R., 2006, *ApJ*, **640**, L43
- Sollima A., Ferraro F. R., Pancino E., Bellazzini M., 2008, *Mem. Soc. Astron. Italiana*, **79**, 342
- Stetson P. B., 1987, *PASP*, **99**, 191
- Stetson P. B., 1994, *PASP*, **106**, 250
- Tailo M., Di Criscienzo M., D'Antona F., Caloi V., Ventura P., 2016, *MNRAS*, **457**, 107
- Villanova S., Geisler D., Gratton R. G., Cassisi S., 2014, *ApJ*, **791**, 107
- Wright E. L., et al., 2010, *AJ*, **140**, 1868

## APPENDIX A: RRL PHOTOMETRY

Table A1: Parameters for 99 RRLs in  $\omega$  Cen. First five columns are star ID, right ascension and declination, pulsation mode, and period in days from Kaluzny et al. (2004). Columns 6 through 11 are  $JHK_s$  apparent magnitudes and errors from FourStar data. Columns 12 through 17 are  $3.6\ \mu\text{m}$  and  $4.5\ \mu\text{m}$  apparent magnitudes, errors, and PL residuals ( $\Delta[3.6]$  and  $\Delta[4.5]$ ) from IRAC data. Columns 18–21 are photometric ([Fe/H], p) and spectroscopic ([Fe/H], s) metallicities and errors from Rey et al. (2000) and Sollima et al. (2006) respectively.

ID	RA (J2000)	Dec (J2000)	Mode	$P$ (days)	$J$	$\sigma_J$	$H$	$\sigma_H$	$K_s$	$\sigma_{K_s}$	[3.6]	$\sigma_{[3.6]}$	$\Delta[3.6]$	[4.5]	$\sigma_{[4.5]}$	$\Delta[4.5]$	[Fe/H], p	$\sigma_{[\text{Fe}/\text{H}]}, \text{p}$	[Fe/H], s	$\sigma_{[\text{Fe}/\text{H}]}, \text{s}$
3	13:25:56.15	-47:25:53.8	RRab	0.841	13.247	0.017	12.982	0.018	12.882	0.017	12.841	0.039	-0.087	12.708	0.036	0.035	-1.540	0.050	—	—
4	13:26:12.93	-47:24:18.8	RRab	0.627	13.475	0.016	13.219	0.021	13.133	0.020	13.030	0.036	0.026	13.026	0.035	0.016	-1.740	0.050	—	—
5	13:26:18.33	-47:23:12.4	RRab	0.515	13.700	0.017	13.549	0.020	13.507	0.027	13.387	0.043	-0.129	13.340	0.030	-0.096	-1.350	0.080	-1.240	0.110
7	13:27:00.90	-47:14:00.5	RRab	0.713	13.333	0.009	13.151	0.031	13.036	0.018	—	—	—	—	—	—	-1.460	0.080	—	—
8	13:27:48.45	-47:28:20.3	RRab	0.521	13.505	0.015	13.258	0.017	13.223	0.014	—	—	—	—	—	—	-1.910	0.280	—	—
9	13:25:59.58	-47:26:24.0	RRab	0.523	13.776	0.017	13.534	0.021	13.470	0.016	13.315	0.036	-0.072	13.279	0.039	-0.051	-1.490	0.060	—	—
10	13:26:06.99	-47:24:36.6	RRc	0.375	13.579	0.014	13.395	0.023	13.345	0.019	13.342	0.037	-0.026	13.168	0.037	0.112	-1.660	0.100	—	—
11	13:26:30.59	-47:23:01.6	RRab	0.565	13.481	0.014	13.307	0.028	13.219	0.025	13.050	0.058	—	—	—	—	-1.670	0.130	-1.610	0.220
12	13:26:27.21	-47:24:06.2	RRc	0.387	13.590	0.018	13.379	0.028	13.305	0.025	13.168	0.048	0.112	13.448	0.088	-0.208	-1.530	0.140	—	—
13	13:25:58.18	-47:25:21.6	RRab	0.669	13.353	0.019	13.081	0.022	13.058	0.017	12.918	0.032	0.072	12.860	0.031	0.117	-1.910	0.000	—	—
14	13:25:59.74	-47:39:09.6	RRc	0.377	13.588	0.011	13.343	0.020	13.365	0.016	—	—	—	13.299	0.045	—	-1.710	0.130	—	—
15	13:26:27.11	-47:24:38.0	RRab	0.811	13.245	0.018	13.020	0.031	12.954	0.025	13.149	0.084	—	—	—	—	-1.640	0.390	-1.680	0.180
16	13:27:37.69	-47:37:34.8	RRc	0.330	13.680	0.015	13.502	0.022	13.437	0.018	—	—	—	—	—	—	-1.290	0.080	-1.650	0.460
18	13:27:45.11	-47:24:56.6	RRab	0.622	13.371	0.010	13.131	0.024	13.100	0.016	13.006	0.043	—	—	—	—	-1.780	0.280	—	—
20	13:27:14.05	-47:28:06.3	RRab	0.616	13.410	0.015	13.210	0.036	13.125	0.025	13.060	0.039	0.016	12.940	0.029	0.122	—	—	-1.520	0.340
21	13:26:11.17	-47:25:58.8	RRc	0.381	13.578	0.016	13.399	0.027	13.361	0.020	13.301	0.047	-0.003	13.200	0.032	0.061	-0.900	0.110	—	—
22	13:27:41.04	-47:34:07.6	RRc	0.396	13.572	0.012	13.380	0.016	13.288	0.017	—	—	—	—	—	—	-1.630	0.170	-1.600	0.990
23	13:26:46.50	-47:24:39.5	RRab	0.511	13.941	0.025	13.794	0.048	13.658	0.033	13.325	0.064	—	—	—	—	-1.080	0.140	-1.350	0.580
24	13:27:38.32	-47:34:14.5	RRc	0.462	13.419	0.012	13.218	0.014	13.138	0.014	—	—	—	—	—	—	-1.860	0.030	—	—
30	13:26:15.94	-47:29:56.0	RRc	0.404	13.521	0.021	13.287	0.046	13.251	0.030	13.188	0.047	0.041	13.071	0.060	0.112	-1.750	0.170	-1.620	0.280
32	13:27:03.32	-47:21:38.9	RRab	0.620	13.508	0.009	13.244	0.018	13.132	0.018	—	—	—	—	—	—	-1.530	0.160	—	—
33	13:25:51.60	-47:29:05.8	RRab	0.602	13.338	0.015	13.106	0.022	13.091	0.019	—	—	—	13.006	0.035	—	-2.090	0.230	-1.580	0.420
34	13:26:07.21	-47:33:10.4	RRab	0.734	13.273	0.014	13.018	0.014	12.916	0.013	—	—	—	12.838	0.065	—	-1.710	0.000	—	—
35	13:26:53.21	-47:22:34.7	RRc	0.387	13.586	0.012	13.463	0.024	13.356	0.023	—	—	—	—	—	—	-1.560	0.080	-1.630	0.360
36	13:27:10.11	-47:15:29.8	RRc	0.380	13.534	0.007	13.372	0.019	13.307	0.014	—	—	—	—	—	—	-1.490	0.230	—	—
38	13:27:03.30	-47:36:30.2	RRab	0.779	13.226	0.015	12.943	0.019	12.814	0.018	—	—	—	—	—	—	-1.750	0.180	-1.640	0.400
39	13:27:59.77	-47:34:42.3	RRc	0.393	13.560	0.009	13.415	0.014	13.308	0.014	—	—	—	—	—	—	-1.960	0.290	—	—
40	13:26:24.56	-47:30:46.2	RRab	0.634	13.517	0.022	13.250	0.051	13.153	0.033	13.062	0.049	-0.017	13.416	0.056	-0.385	-1.600	0.080	-1.620	0.190
44	13:26:22.39	-47:34:35.3	RRab	0.568	13.677	0.014	13.425	0.023	13.368	0.018	—	—	—	13.132	0.036	—	-1.400	0.120	-1.290	0.350
45	13:25:30.88	-47:27:21.0	RRab	0.589	13.513	0.015	13.201	0.015	13.164	0.014	—	—	—	13.070	0.028	—	-1.780	0.250	—	—
46	13:25:30.23	-47:25:51.8	RRab	0.687	13.299	0.016	12.998	0.017	12.947	0.014	—	—	—	—	—	—	-1.880	0.170	—	—
47	13:25:56.46	-47:24:12.0	RRc	0.485	13.420	0.020	13.223	0.018	13.150	0.018	13.099	0.030	-0.080	13.073	0.026	-0.126	-1.580	0.310	—	—
49	13:26:07.78	-47:37:55.5	RRab	0.605	13.566	0.012	13.238	0.019	13.220	0.016	—	—	—	13.099	0.049	—	-1.980	0.110	—	—
50	13:25:53.94	-47:27:35.8	RRc	0.386	13.647	0.014	13.402	0.015	13.362	0.014	—	—	—	13.305	0.056	—	-1.590	0.190	—	—
51	13:26:42.66	-47:24:21.4	RRab	0.574	13.597	0.014	13.378	0.033	13.270	0.029	13.315	0.083	—	—	—	—	-1.640	0.210	-1.840	0.230
54	13:26:23.54	-47:18:47.7	RRab	0.773	13.281	0.016	12.998	0.017	12.954	0.015	12.799	0.030	—	—	—	—	-1.660	0.120	-1.800	0.230
56	13:25:55.53	-47:37:44.1	RRab	0.568	13.643	0.009	13.386	0.022	13.353	0.017	—	—	—	13.232	0.035	—	-1.260	0.150	—	—
57	13:27:49.38	-47:36:50.5	RRab	0.794	13.234	0.015	12.995	0.018	12.882	0.014	—	—	—	—	—	—	-1.890	0.140	—	—
58	13:26:13.05	-47:24:03.0	RRc	0.370	13.660	0.017	13.495	0.018	13.421	0.021	13.345	0.033	-0.013	13.309	0.034	-0.011	-1.370	0.180	-1.910	0.310
59	13:26:18.43	-47:29:46.7	RRab	0.519	13.727	0.023	13.424	0.043	13.391	0.033	13.248	0.071	0.004	13.418	0.064	-0.181	-1.000	0.280	—	—
63	13:25:07.96	-47:36:54.1	RRab	0.826	13.223	0.017	12.862	0.017	12.869	0.012	—	—	—	—	—	—	-1.730	0.090	—	—
64	13:26:02.22	-47:36:19.2	RRc	0.344	13.638	0.013	13.438	0.022	13.407	0.022	—	—	—	13.314	0.044	—	-1.460	0.230	—	—
66	13:26:33.08	-47:22:25.2	RRc	0.407	13.542	0.011	13.359	0.022	13.264	0.020	13.103	0.035	—	—	—	—	-1.680	0.340	—	—
67	13:26:28.62	-47:18:46.9	RRab	0.564	13.610	0.014	13.384	0.016	13.326	0.015	13.368	0.047	—	—	—	—	-1.100	0.000	-1.190	0.230
68	13:26:12.80	-47:19:35.7	RRc	0.535	13.258	0.021	13.004	0.015	12.970	0.015	12.928	0.050	—	—	—	—	-1.600	0.010	—	—
69	13:25:11.02	-47:37:33.5	RRab	0.635	—	—	—	—	13.112	0.014	—	—	—	—	—	—	-1.520	0.140	—	—
70	13:27:27.76	-47:33:42.7	RRc	0.391	13.529	0.013	13.282	0.029	13.254	0.022	—	—	—	—	—	—	-1.940	0.150	-1.740	0.300
72	13:27:33.11	-47:16:22.9	RRc	0.385	13.554	0.010	13.339	0.017	13.311	0.014	—	—	—	—	—	—	-1.320	0.220	—	—
73	13:25:53.75	-47:16:10.8	RRab	0.575	13.480	0.018	13.251	0.017	13.215	0.016	—	—	—	—	—	—	-1.500	0.090	—	—
74	13:27:07.22	-47:17:33.9	RRab	0.503	13.622	0.008	13.457	0.016	13.405	0.015	—	—	—	—	—	—	-1.830	0.360	—	—
75	13:27:19.70	-47:18:46.5	RRc	0.422	13.410	0.011	13.175	0.028	13.137	0.025	—	—	—	—	—	—	-1.490	0.080	-1.820	0.990
76	13:26:57.23	-47:20:07.7	RRc	0.338	13.634	0.012	13.488	0.017	13.449	0.020	—	—	—	—	—	—	-1.450	0.130	—	—
77	13:27:20.89	-47:22:05.6	RRc	0.426	13.474	0.013	13.264	0.028	13.199	0.021	—	—	—	—	—	—	-1.810	0.000	-1.840	0.430

Continued on next page



Table A1 - *Continued from previous page*

ID	RA (J2000)	Dec (J2000)	Mode	$P$ (days)	$J$	$\sigma_J$	$H$	$\sigma_H$	$K_s$	$\sigma_{K_s}$	[3.6]	$\sigma_{[3.6]}$	$\Delta[3.6]$	[4.5]	$\sigma_{[4.5]}$	$\Delta[4.5]$	[Fe/H], p	$\sigma_{[\text{Fe}/\text{H}]}$ , p	[Fe/H], s	$\sigma_{[\text{Fe}/\text{H}]}$ , s
79	13:28:24.99	-47:29:25.2	RRab	0.608	13.382	0.010	13.162	0.016	13.123	0.015	—	—	—	—	—	—	-1.390	0.180	—	—
81	13:27:36.68	-47:24:48.3	RRc	0.389	13.542	0.013	13.326	0.033	13.286	0.025	13.248	0.076	—	—	—	—	-1.720	0.310	-1.990	0.430
82	13:27:35.61	-47:26:30.3	RRc	0.336	13.579	0.016	13.324	0.024	13.296	0.018	—	—	—	13.827	0.104	—	-1.560	0.200	-1.710	0.560
83	13:27:08.42	-47:21:34.1	RRc	0.357	13.603	0.010	13.431	0.024	13.370	0.022	—	—	—	—	—	—	-1.300	0.220	—	—
84	13:24:47.45	-47:29:56.5	RRab	0.580	—	—	12.833	0.017	12.781	0.016	—	—	—	—	—	—	-1.470	0.100	—	—
85	13:25:06.49	-47:23:34.0	RRab	0.743	13.344	0.011	—	—	—	—	—	—	—	—	—	—	-1.870	0.310	—	—
94	13:25:57.06	-47:22:46.1	RRc	0.254	14.070	0.024	13.934	0.022	13.870	0.027	13.858	0.038	-0.092	13.799	0.029	-0.014	-1.000	0.110	—	—
95	13:25:24.95	-47:28:53.2	RRc	0.405	13.497	0.015	13.269	0.017	13.264	0.017	—	—	—	13.178	0.024	—	-1.840	0.550	—	—
97	13:27:08.49	-47:25:30.9	RRab	0.692	13.302	0.010	13.143	0.029	13.034	0.022	12.964	0.061	-0.008	12.702	0.064	0.240	-1.560	0.370	-1.740	0.170
101	13:27:30.24	-47:29:51.0	RRc	0.341	13.708	0.016	13.484	0.030	13.436	0.023	—	—	—	—	—	—	-1.880	0.320	—	—
102	13:27:22.11	-47:30:12.3	RRab	0.691	13.320	0.012	13.033	0.022	12.993	0.020	12.984	0.049	-0.028	13.056	0.072	-0.113	-1.840	0.130	-1.650	0.160
103	13:27:14.29	-47:28:36.3	RRc	0.329	13.620	0.018	13.409	0.040	13.377	0.034	12.960	0.071	—	13.024	0.066	—	-1.920	0.110	-1.780	0.270
104	13:28:07.76	-47:33:44.9	RRab	0.867	13.732	0.096	13.626	0.154	13.452	0.141	—	—	—	—	—	—	-1.830	0.180	—	—
105	13:27:46.02	-47:32:43.9	RRc	0.335	13.768	0.014	13.615	0.020	13.533	0.018	—	—	—	—	—	—	-1.240	0.180	—	—
107	13:27:14.05	-47:30:57.9	RRab	0.514	13.597	0.017	13.340	0.038	13.301	0.030	13.535	0.219	—	13.351	0.076	—	-1.360	0.110	—	—
115	13:26:12.30	-47:34:17.5	RRab	0.630	13.401	0.012	13.176	0.017	13.103	0.013	—	—	—	—	—	—	-1.870	0.010	-1.640	0.320
117	13:26:19.91	-47:29:21.0	RRc	0.422	13.480	0.020	13.274	0.043	13.202	0.031	13.110	0.044	0.071	12.949	0.043	0.179	-1.680	0.250	—	—
120	13:26:25.52	-47:32:48.6	RRab	0.549	13.525	0.049	13.072	0.079	13.135	0.094	12.958	0.066	0.236	12.927	0.055	0.253	-1.390	0.060	-1.150	0.160
121	13:26:28.17	-47:31:50.5	RRc	0.304	13.741	0.016	13.648	0.033	13.531	0.026	13.414	0.037	0.144	13.302	0.033	0.249	-1.460	0.130	-1.830	0.400
122	13:26:30.31	-47:33:02.2	RRab	0.635	13.369	0.018	13.132	0.042	13.062	0.024	13.057	0.052	-0.013	12.987	0.052	0.043	-2.020	0.180	-1.790	0.210
123	13:26:51.17	-47:37:13.2	RRc	0.474	13.462	0.016	13.239	0.019	13.174	0.017	—	—	—	—	—	—	-1.640	0.010	—	—
124	13:26:54.49	-47:39:07.5	RRc	0.332	13.708	0.013	13.510	0.018	13.482	0.023	—	—	—	—	—	—	-1.330	0.230	—	—
125	13:26:48.92	-47:41:03.7	RRab	0.593	13.420	0.015	13.200	0.016	13.153	0.015	—	—	—	—	—	—	-1.670	0.220	-1.810	0.380
126	13:28:08.03	-47:40:46.7	RRc	0.342	13.642	0.011	13.467	0.017	13.370	0.016	—	—	—	—	—	—	-1.310	0.130	—	—
127	13:25:19.36	-47:28:37.6	RRc	0.305	—	—	—	—	13.579	0.018	—	—	—	13.573	0.063	—	-1.590	0.080	—	—
128	13:26:17.75	-47:30:13.0	RRab	0.835	13.207	0.018	12.927	0.032	12.810	0.020	—	—	—	12.445	0.074	—	-1.880	0.040	—	—
130	13:26:09.93	-47:13:40.0	RRab	0.493	13.688	0.021	13.527	0.032	13.418	0.025	—	—	—	—	—	—	-1.460	0.170	—	—
147	13:27:15.86	-47:31:09.2	RRc	0.423	13.397	0.012	12.934	0.041	13.083	0.022	—	—	—	12.585	0.096	—	-1.660	0.140	—	—
149	13:27:32.94	-47:13:43.6	RRab	0.683	13.354	0.015	13.061	0.035	13.024	0.024	—	—	—	—	—	—	-1.210	0.240	—	—
150	13:27:40.21	-47:36:00.1	RRab	0.899	13.068	0.019	12.757	0.025	12.692	0.018	—	—	—	—	—	—	-1.760	0.340	—	—
151	13:28:25.40	-47:16:00.2	RRab	0.408	13.501	0.013	13.301	0.020	13.265	0.016	—	—	—	—	—	—	-1.300	0.240	—	—
163	13:25:49.42	-47:20:21.5	RRc	0.313	13.763	0.019	13.557	0.016	13.545	0.025	—	—	—	—	—	—	-1.180	0.270	—	—
168	13:25:52.78	-47:32:02.9	RRc	0.321	14.176	0.015	14.000	0.020	13.960	0.018	—	—	—	—	—	—	—	—	—	—
169	13:27:20.47	-47:23:59.1	RRc	0.319	13.805	0.013	13.735	0.019	13.652	0.025	13.734	0.050	-0.232	14.001	0.116	-0.512	—	—	-1.650	0.190
184	13:27:28.50	-47:31:35.4	RRc	0.303	13.778	0.012	13.624	0.028	13.536	0.019	—	—	—	—	—	—	—	—	—	—
185	13:26:04.13	-47:21:45.0	RRc	0.333	13.701	0.016	13.545	0.018	13.508	0.023	13.496	0.036	-0.043	13.479	0.033	-0.046	—	—	—	—
261	13:27:15.41	-47:21:29.5	RRc	0.403	13.431	0.009	13.212	0.019	13.113	0.020	—	—	—	—	—	—	—	—	-1.500	0.350
263	13:26:13.13	-47:26:09.7	RRab	1.012	13.155	0.017	12.888	0.017	12.746	0.016	—	—	—	12.660	0.034	—	—	—	-1.730	0.190
274	13:26:43.73	-47:22:48.2	RRc	0.311	13.828	0.011	13.758	0.023	13.650	0.022	—	—	—	—	—	—	—	—	—	—
276	13:27:16.51	-47:33:17.6	RRc	0.308	13.727	0.021	13.614	0.046	13.533	0.024	—	—	—	—	—	—	—	—	—	—
280	13:27:09.33	-47:23:05.7	RRc	0.282	13.951	0.012	13.905	0.026	13.816	0.029	—	—	—	—	—	—	—	—	—	—
285	13:25:40.20	-47:34:48.4	RRc	0.329	13.687	0.017	13.504	0.027	13.503	0.015	—	—	—	13.358	0.074	—	—	—	—	—
288	13:28:10.32	-47:23:47.8	RRc	0.295	13.809	0.011	13.719	0.016	13.635	0.019	—	—	—	—	—	—	—	—	—	—
289	13:28:03.68	-47:21:27.9	RRc	0.308	13.743	0.013	13.618	0.015	13.584	0.022	—	—	—	—	—	—	—	—	—	—
291	13:26:38.52	-47:33:28.0	RRc	0.334	13.674	0.018	13.518	0.044	13.444	0.026	—	—	—	—	—	—	—	—	—	—
357	13:26:17.77	-47:30:23.4	RRc	0.298	13.692	0.027	13.468	0.064	13.468	0.045	13.462	0.044	0.120	13.375	0.041	0.204	—	—	-1.640	0.990

This paper has been typeset from a  $\text{\TeX/L\AA\TeX}$  file prepared by the author.